Research Article Vol. 34, No. 3 / 9 Feb 2026 / Optics Express 4418

Optics EXPRESS

High-resolution profiling of aerosol absorption coefficients using dual-polarization lidar and a PSO–GPR machine learning approach

QINGQING DONG, ZHONGWEI HUANG,* QIANTAO LIU, YONGKAI WANG, ZHENGPENG LI, JIANRONG BI, TIAN ZHOU, AND JINSEN SHI

Key Laboratory of Semi-Arid Climate Changes with the Ministry of Education, College of Atmospheric Sciences, Lanzhou University, Lanzhou 730000, China
huangzhongwei@lzu.edu.cn

Abstract: The aerosol absorption coefficient (AAC) is of great importance to quantify aerosol radiative forcing and associated impacts on the climate. However, reliable vertical profiles of AAC remain limited, as most existing methods are restricted to surface observations or columnar estimates. This study develops a new approach to retrieving vertical profiles of AAC from dual-polarization lidar measurements, which can simultaneously detect polarization ratios both at 355 nm and 532 nm. The approach integrates a particle swarm optimization–Gaussian process regression (PSO-GPR) scheme with in-situ absorption observations collected in Northwest China. The lidar-retrieved AAC values near the surface show good agreement with co-located Aethalometer measurements. Moreover, comparisons with tethered balloon observations indicate a correlation coefficient of 0.74 for vertical profiles, confirming the robustness of the approach. This work presents an effective and practical method for obtaining reliable, high-resolution AAC profiles from remote sensing, offering new opportunities for evaluating aerosol radiative impacts with improved accuracy.

1. Introduction

Atmospheric aerosols play a crucial role in affecting the radiation energy budget of the Earth-atmosphere system by the mechanisms of shortwave and longwave radiation scattering and absorption [1,2]. Absorbing aerosols can increase atmospheric temperatures by intercepting solar radiation, which decreases relative humidity and reduces cloud cover [3,4]. This radiative heating modifies the near-surface thermodynamic structure, enhancing atmospheric stability in the lower layers and suppressing boundary layer development and convective activity [5]. Moreover, such thermal forcing has the ability to modify major hydrological cycles and patterns of rainfall and thus has profound impacts on regional climates [6,7].

The aerosol absorption coefficient (AAC), defined as the capacity of radiative absorption by aerosols across all wavelengths, is one of the key parameters used in quantifying atmospheric radiation and in aerosol modelling [8–10]. The major contributors to aerosol solar radiation absorption are the carbonaceous aerosols, such as elemental carbon and organic carbon, and mineral dust [11,12]. Xu et al. [13] suggested that black carbon (BC) radiative absorption is one of the major factors in atmospheric extinction and that $PM_{2.5}$ (particulate matter with diameter $\leq$ 2.5 μm) and BC are the major pollutants that cause haze in Shanghai. Dust aerosols also play an important role, particularly in absorbing solar radiation in the near-ultraviolet and blue light regions, exhibiting a stronger wavelength dependence than BC [14–16]. Notably, dust aerosols may account for over 50% of the total absorbing aerosol optical depth at 550 nm [17]. Sokolik and Toon [18] pointed out that the absorption and refractive index of dust aerosols are affected by factors such as particle size distribution, composition, and shape. The absorption and reflection

#587704 https://doi.org/10.1364/OE.587704
Journal © 2026 Received 15 Dec 2025; revised 18 Jan 2026; accepted 20 Jan 2026; published 29 Jan 2026

Optics EXPRESS

properties of dust aerosols can impact the thermal structure of the atmosphere, thereby impacting atmospheric circulation.

Accurate AAC measurements are essential for atmospheric studies, but remain challenging. Filter-based techniques, widely used in instruments such as Aethalometer, multi-angle absorption photometer (MAAP), and particle soot absorption photometer (PSAP), assess optical properties of collected aerosols on filter membranes [19–21]. However, the unique structure of the filter membrane fibers can cause cross-sectional sensitivity problems with possible resulting inaccurate measurements [22]. Moreover, conventional measurement platforms typically provide AAC data only at fixed altitudes, while aerosols at different heights affect radiative transfer differently [23]. Vertical profiling of optical aerosol characteristics is still technologically challenging due to the inherent constraints of traditional platforms used in measurements. Much effort has been given towards the advancement of vertical sampling methods, such as tethered balloons and unmanned aerial vehicles (UAVs) with onboard meteorology sensors [24]. Nevertheless, these methods still face persistent challenges, such as prohibitively expensive operating costs, restricted temporal and spatial resolution, and limited maximum sampling altitudes. Therefore, high-precision characterization of vertical distributions of AAC remains a challenge to atmospheric scientists.

Remote sensing techniques have advanced substantially in recent decades, enabling observations of aerosol physical and chemical properties as well as spatiotemporal variability [25]. Lidar, in particular, provides vertically resolved aerosol profiling and is widely used to retrieve aerosol optical properties [26]. Various inversion algorithms have been developed using high-quality lidar data to extract vertical profiles of aerosol characteristics [27,28]. Huang et al. [29] proposed the possibility of retrieving AAC by applying dual-polarization lidar.

With increasing availability of observational and model datasets and enhanced computational power, machine learning approaches have emerged as effective tools in atmospheric studies. In this work, we propose a hybrid machine learning approach, combining particle swarm optimization (PSO) with Gaussian process regression (GPR), to retrieve AAC from lidar measurements. PSO is used to optimize hyperparameters, while GPR performs probabilistic predictions using the optimized parameters [30,31]. This combined framework leverages evolutionary optimization and non-parametric regression, improving retrieval accuracy. Using dual-polarization lidar measurements, we obtain high-resolution vertical profiles of AAC, which are validated against ground-based sensors and tethered balloon observations. This study demonstrates a practical and scalable approach for accurate characterization of aerosol absorption in the lower atmosphere. Section 2 introduces the study site, instruments, and methodology. Section 3 describes the retrieval methodology and validation results. Section 4 presents the discussion.

2. Instruments and methodology

2.1. Field experiment

To investigate the vertical distribution and microphysical properties of dust aerosols in the source region, field campaigns were conducted at the Linze (39.1°N, 100.2°E, 1578 m.a.s.l) and Minqin (38.6°N, 103.0°E, 1384 m.a.s.l) stations. In Fig. 1, these stations are located in different dust source regions, with Linze situated to the southwest of the Badain Jaran Desert and Minqin positioned between two major desert systems: the Badain Jaran Desert to the northwest and the Tengger Desert to the southeast.

The experimental design incorporated advanced instrumentation and multi-platform measurement strategies to ensure comprehensive data acquisition. At Linze, a dual-polarization lidar was deployed in April 2014 to provide continuous vertical profiles of aerosols and clouds, complemented by ground-level AAC measurements from a MAAP. At Minqin, observations were conducted in two phases: (1) Ground-based observations from March 14 to March 22, 2021, using a dual-polarization lidar for profiling aerosol vertical distribution and an AE33

Optics EXPRESS

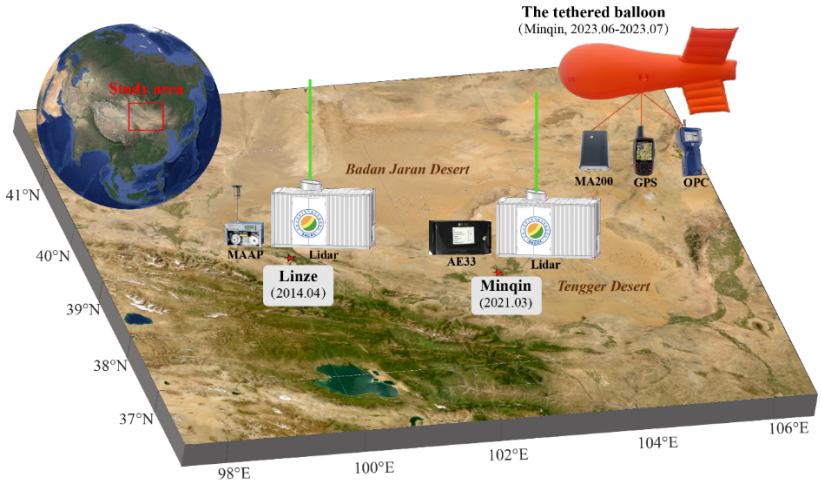

Fig. 1. Locations of field experiment sites and instrument configuration used in this study. Linze Station was equipped with a dual-polarization lidar and a MAAP. The Minqin Station featured two observational platforms: (1) ground-based measurements using a dual-polarization lidar and an AE33 Aethalometer; and (2) tethered balloon platform equipped with a microAeth MA200, a GPS tracker, and an OPC.

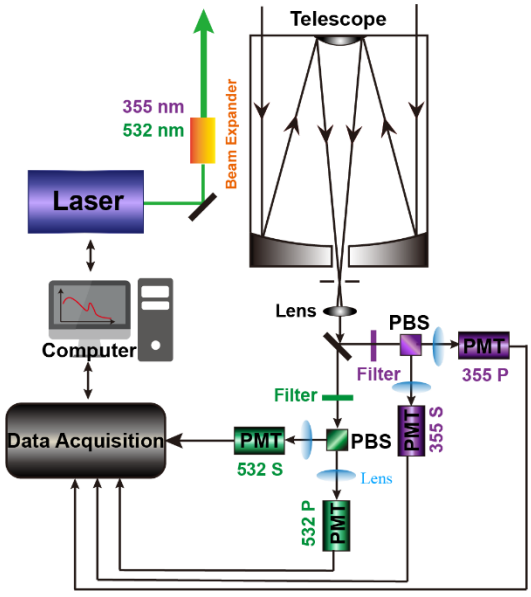

Fig. 2. Schematic of developed dual-polarization lidar system in this study.

aethalometer for near-surface AAC; (2) Tethered balloon observations from June 26 to July 6, 2022, equipped with a portable MA200 aethalometer.

2.2. *Dual-polarization lidar system*

The dual-polarization lidar system used in this study (Fig. 2) was independently developed by Lanzhou University, China. It consists of three main components: the transmitting module, the receiving module, and the data acquisition module [32–34]. The transmitter employs a Nd: YAG

Optics EXPRESS

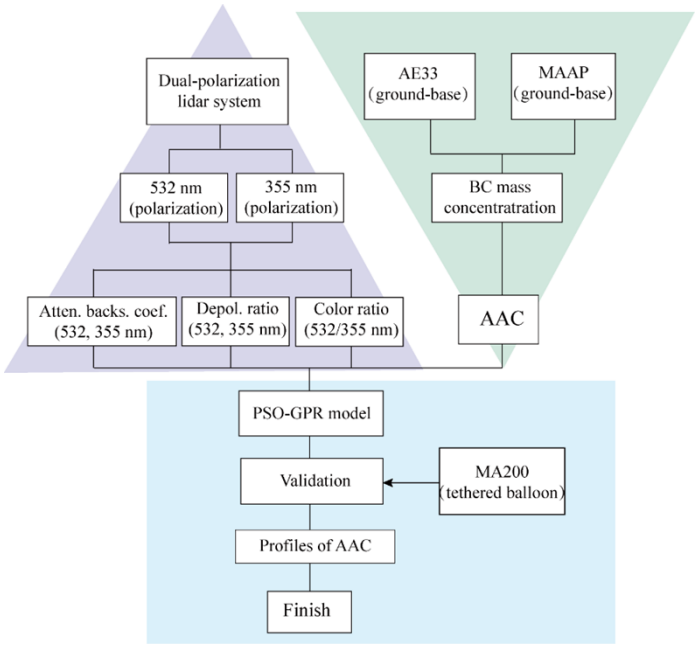

Fig. 3. Flowchart for retrieving AAC profiles from polarization lidar measurements based on the PSO-GPR model.

laser operating at wavelengths of 355 and 532 nm, with a pulse energy of 100 mJ at 532 nm and a repetition rate of 10 Hz. Backscattered signals are collected by a 400 mm Cassegrain telescope and separated into vertical and horizontal polarization components by a polarization beam splitter (PBS), which are detected by photomultiplier tubes (PMTs). The system provides a vertical resolution of 7.5 m and a temporal resolution of 3 min. Output products include backscatter coefficient, depolarization ratio at two wavelengths (532 nm and 355 nm), and color ratio. These parameters serve as key indicators for characterizing aerosol optical properties and for retrieving AACs in this study. The attenuated backscatter coefficient serves as a proxy for aerosol concentration, while the depolarization ratio is highly sensitive to particle shape, effectively distinguishing non-spherical dust from spherical pollutants. Additionally, the color ratio provides information related to particle size distribution. These parameters were chosen to maximize the model's ability to capture variations in AAC.

2.3. AAC detection

AAC and BC concentrations were measured using two filter-based optical instruments: the seven-wavelength Aethalometer AE33 (Magee Scientific, USA) and the five-wavelength microAeth MA200 (AethLabs, USA). Both instruments determine particle light absorption through real-time optical attenuation on filters, applying a dual-spot compensation scheme to correct for filter-loading artifacts [20,35,36]. The AE33 is widely used for long-term ground-based monitoring, while the lightweight MA200 is better suited for mobile platforms such as tethered balloons. Validation studies under controlled conditions have demonstrated strong consistency between the two instruments ($R^2 > 0.9$) [37,38].

Because of the relatively clean background during balloon soundings and the high temporal resolution of MA200 data, the raw signals often exhibited reduced signal-to-noise ratios with more outliers. To address this, an optimized noise-reduction averaging (ONA) algorithm was applied in data processing [39].

Optics EXPRESS

MAAP (Thermo Scientific, USA) is the most reliable filter-based instrument used to measure the mass concentration of AAC and BC at 637 nm with high precision. Unlike traditional filter-based methods, the MAAP uses multi-angle light absorption photometry along with radiative transfer modeling to correct for multiple scattering [40,41]. Although it operates at a single wavelength (637 nm), its results are comparable to those from aethalometers in the red channel. [42–44]. In this study, BC mass concentration is converted to AAC using an empirical conversion factor of 6.6 m^2/g [45].

2.4. Tethered balloon observations

The tethered balloon serves as an airborne platform specifically engineered to carry meteorological detection equipment, thereby functioning as an effective instrument for the in-situ vertical profiling of atmospheric aerosols and meteorological parameters. The tethered balloon, filled with 6 m^3 of helium and carrying up to 5 kg payload, was operated with an electric winch at an ascent rate of 1.0 ± 0.2 m s^{-1}, reaching altitudes of ~1200 m above ground level. The tethered airship was equipped with: (1) a KZXLT-II weather sensor to measure meteorological parameters (pressure, temperature, wind direction and wind speed); (2) a microAeth MA200 (AethLabs, USA) for AAC detection; (3) an optical particle counter (OPC, TSI 9306, USA) for particle number concentration (0–10 μm); and (4) a GPS Tracker (Garmin, USA) for real-time altitude and geographical location.

2.5. PSO-GPR method

The rapid development of artificial intelligence (AI) has resulted in the extensive use of machine learning techniques in nearly all fields. GPR has proven to be a robust probabilistic modeling system based on Bayesian principles and statistical learning principles [46]. GPR is also highly effective in handling sophisticated regression and classification problems that are marked by high-dimensional, small-sample, and nonlinear data types and exhibits excellent adaptability and generalization [31,47]. Along with probabilistic methods, evolutionary computing methods like PSO offer powerful solutions for global optimization problems. PSO, developed from the swarm foraging behavior of flocks of birds, uses a population-based search strategy in which candidate solutions (i.e., termed as particles) iteratively move toward ideal regions through social information and individual experience sharing [30,48]. The strategy converges very fast while ensuring robustness to local optima [49,50].

GPR usually requires heavy computational resources, and hyperparameter optimization becomes crucial in order to improve the accuracy of the predictions. Conventional methodologies that rely on conjugate gradient (CG) optimization suffer from suboptimal convergence due to sensitivity to the initial choice of parameters and susceptibility to local minima [51]. These constraints highlight the importance of developing more robust optimization methods. This research introduces a PSO-GPR model framework that aims to resolve these issues by hybridizing evolutionary computation with probabilistic modeling. Here, the role of the PSO algorithm is that of the hyperparameter optimization component, while that of the GPR model is prediction-making using the best set of parameters [52]. The application of the PSO-GPR has the dual advantage of minimizing the overhead in computations by mitigating the number of iterations in training and improving the generalizability of the model with better hyperparameter selection [53,54]. Based on preliminary evaluations and theoretical principles, the PSO-GPR framework was selected over conventional machine learning methods due to its superior ability to avoid local minima and its robustness in handling small-sample, non-linear inversion problems. This ensures optimal hyperparameter tuning and retrieval accuracy, making it highly suitable for the specific application and validation targets of this study.

By synergistically integrating ground-based and sounding observations with the PSO-GPR model, the high-resolution vertical profiles of AAC were derived (Fig. 3). Building on the

Optics EXPRESS

correlations observed between lidar-derived depolarization ratios and AAC [29], the research expanded the predictive framework by incorporating multiple lidar observables as input features. Specifically, the dual-polarization lidar provides vertical profiles of depolarization ratio, attenuated backscattering coefficients at 532 nm and 355 nm, and color ratio. The model establishes a relationship between these lidar-derived parameters and the AAC, enabling the retrieval of high-resolution AAC vertical profiles.

To validate the model, 25% of the near-surface data, along with half of the sounding data, constituted the validation dataset. The PSO-GPR model framework employed a 2:1 training-testing split, with training samples (N = 2000) and testing samples (N = 1000). This hybrid framework reduced computational cost, improved generalization, and allowed reliable reconstruction of high-resolution AAC profiles from dual-polarization lidar data.

3. Results and discussion

3.1. Aerosol and cloud vertical structures

Coordinated dual-polarization lidar observations were conducted at Linze and Minqin stations to characterize the vertical distribution of aerosols (Fig. 4). The two lidar systems were operated with identical configurations to ensure data comparability.

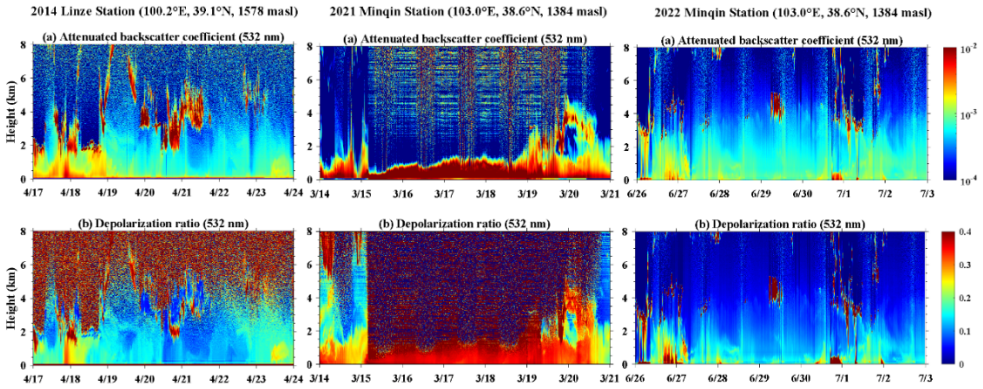

Fig. 4. Vertical distribution of aerosols and clouds from lidar measurements during the field experiments.

During the Linze field campaign in April 2014, lidar observations revealed frequent cloud layers between 2–6 km above ground level, while dust aerosols were largely restricted to the boundary layer (<1 km). Depolarization ratios of 0.26-0.30 indicated the predominance of dust. On April 17, dust intensity increased markedly and remained elevated for several hours. The following day, enhanced convective mixing lifted the dust vertically, bringing it into contact with the cloud base. Between April 19 and 22, the rising boundary layer height contributed to reducing near-surface aerosol concentrations, leading to a gradual decline in dust loading until a new outbreak occurred on April 23. Overall, dust events during this period were relatively weak, remaining confined to the lower troposphere under predominantly cloudy conditions.

At Minqin in March 2021, observations documented a severe spring dust storm. Beginning on March 14, dust was confined below 2 km, with volume depolarization ratios exceeding 0.27. The intensity strengthened steadily, peaking on March 18 with depolarization ratios surpassing 0.35. On March 19, dust concentrations began to decline, while the vertical extent of the layer increased. By March 20, the dust had risen to nearly 5 km, highlighting the dynamic vertical transport of springtime dust in this region. Additional summer measurements at Minqin (2022) confirmed aerosol concentrations were markedly lower than those observed during the spring 2021 storm.

Optics EXPRESS

Nevertheless, dust remained the dominant aerosol type reflecting the station's location within an active dust source region (Fig. 1).

3.2. Training results of the PSO-GPR model

The PSO-GPR model was developed to retrieve vertical profiles of AAC from dual-polarization lidar observations. Its performance was assessed using independent training and testing datasets (Fig. 5). The model showed strong agreement with the 1:1 reference line, achieving R^2 values of 0.97 for the training dataset and 0.90 for the testing dataset. Correspondingly, the Root Mean Square Error (RMSE) was calculated to be 1.08 Mm^{-1} for the training set and 1.95 Mm^{-1} for the testing set. The low RMSE values, relative to the range of AAC variation, further confirm the retrieval accuracy. These results demonstrate that the hybrid PSO-GPR framework can provide robust predictions of AACs, even under dust-laden conditions. Minor underestimations occurred at higher AAC values, particularly in the testing dataset. The consistently high correlations indicate that the evolutionary optimization effectively identified near-optimal hyperparameters, thereby improving the generalizability of the GPR model. This robustness is critical for extending the retrieval framework from surface-level measurements to high-resolution vertical profiles in subsequent analyses.

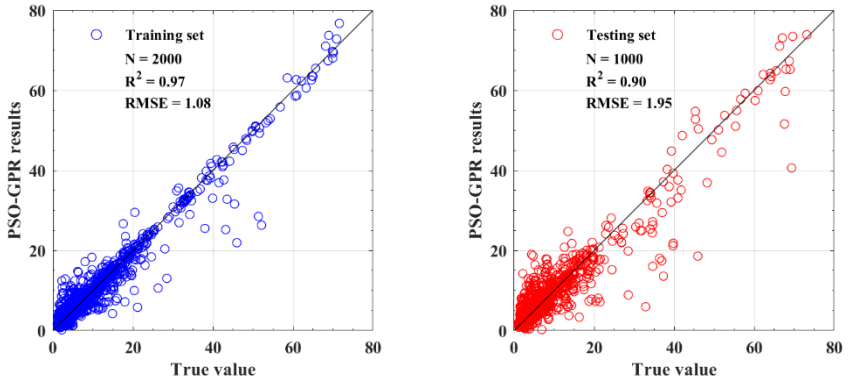

Fig. 5. Comparison between PSO-GPR model results and truth values.

3.3. Tethered balloon observation results

The first sounding, on 28 June, was carried out immediately following a dust event from the previous day. The balloon ascended to its maximum operational altitude of 1000 m AGL within 30 min and was subsequently lowered by an electronic winch to 500 m AGL, where it was maintained for approximately 60 min. Lidar observations (Fig. 6(d)) showed that dust was predominantly confined below 1 km, with depolarization ratios exceeding 0.25, indicative of non-spherical mineral particles. Weak easterly winds (<4 m/s) created stable stratification, limiting both vertical mixing and horizontal dispersion, and resulting in strong aerosol accumulation near the surface. The second sounding on 30 June exhibited a clear contrast. Stronger winds (4–6 m/s) shifted to southerly and southeasterly directions, promoting pollutant dispersion. As a result, near-surface particulate concentrations decreased markedly compared with the 28 June case. Nevertheless, layered structures in the vertical profiles persisted, reflecting incomplete mixing within the boundary layer. The final sounding on 2 July was conducted under relatively clean atmospheric conditions, with depolarization ratios consistently below 0.15. Winds were weak (<4 m/s) from the west to southwest, yet vertical profiles still indicated residual stratification.

As shown in Fig. 7, tethered balloon observations provided vertical profiles of AAC and associated meteorological parameters on 28 and 30 June, and 2 July 2022. The red and black lines

Optics EXPRESS

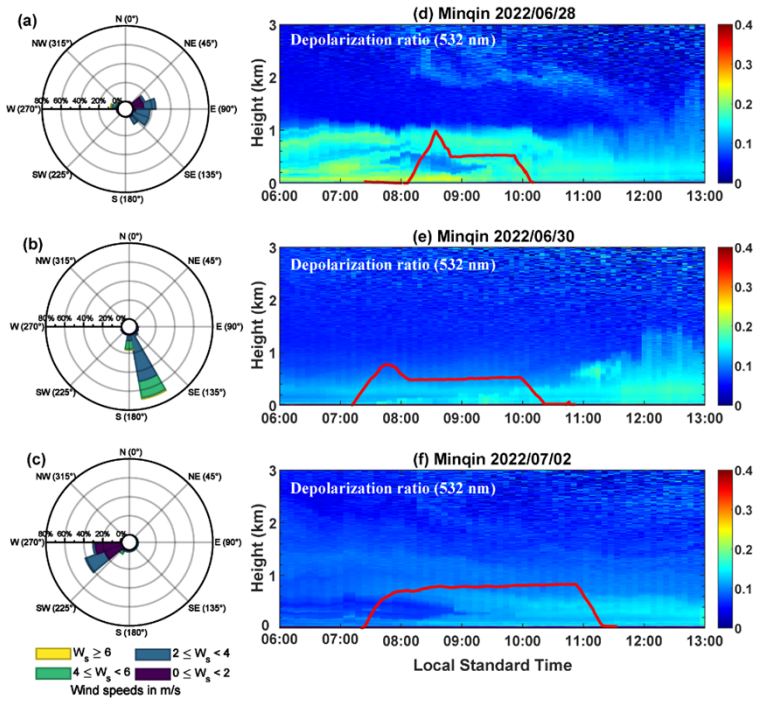

Fig. 6. Three tethered balloon observations: (a)-(c) wind speed and wind direction; (d)-(f) depolarization ratio at 532 nm with balloon height indicated by red lines.

represent ascending and descending profiles, respectively. On June 28, near-surface AAC reached 65 Mm^{-1} and decreased with height to 29 Mm^{-1} at 528 m. OPC measurements revealed multiple concentration peaks at 396 m and 700 m, indicating vertically stratified dust layers. Concurrent meteorological observations at 688 m recorded a temperature increase of approximately 2°C and a humidity decrease of 3%, suggesting that elevated dust layers induced radiative forcing, reducing the downward radiation flux at the surface. During the descent, AAC increased and peaked at 51.3 Mm^{-1} at 418 m before decreasing again. Between 300 m and 400 m, AAC fluctuated around 38 Mm^{-1}, then increased again as the balloon approached the ground.

On 30 June, AAC profiles exhibited relatively high values near the surface during both ascent and descent, with concentrations decreasing gradually with height. The temperature profile during ascent revealed a distinct inversion layer, with the minimum temperature (23.7°C) observed at 280 m. At 10:50 LST, the tethered balloon began its descent from 500 m. By this time, the inversion layer remained evident, and its height had increased. This upward shift is likely attributable to the presence of an absorbing aerosol layer concentrated within the lower boundary layer. The radiative heating induced by these aerosols enhanced convective activity, thereby facilitating boundary-layer growth [55,56].

On 2 July, near-surface AAC reached a peak of 39.4 Mm^{-1} at approximately 100 m above ground level. And due to the precipitation process of the previous day, changes in meteorological elements are more pronounced within 100-200 m. Temperature increased from 18.9°C to 24°C, while relative humidity decreased from 52.7% to 32.8%. As the balloon continued to ascend, the AAC values gradually declined, reaching a minimum of 4.3 Mm^{-1} at 600 m, coinciding with a low particle number concentration of 3.11×10^5 particles. Between 440 m and 530 m, the AAC experienced a slight increase. During the descent, the AAC was approximately 28.5 Mm^{-1} at

Optics EXPRESS

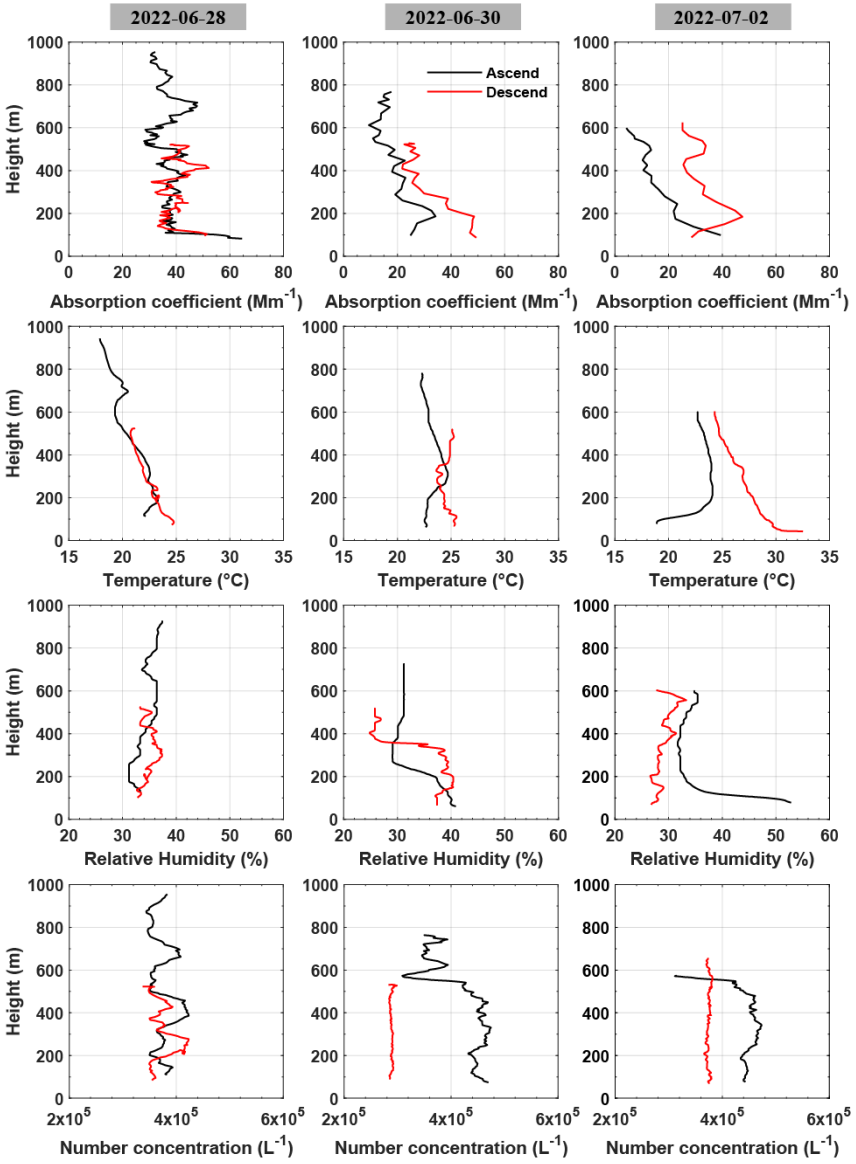

Fig. 7. Vertical profiles of AAC and meteorological parameters from tethered balloon observations. (Note: Red lines represent ascending profiles, while black lines represent descending profiles.)

100 m, reaching a peak of 47.5 Mm^{-1} at 184.5 m. The particle number concentration variations during the descent were minimal, remaining relatively stable at approximately 3.75×10^5 particles.

3.4. Comparison of lidar-retrieved AAC profiles with tethered balloon observations

Figure 8–10 compares AAC profiles retrieved by the PSO-GPR model from dual-polarization lidar measurements with tethered balloon observations. The shaded areas represent the standard deviation of the inversion results, while scatter points denote tethered balloon observations, with blue and orange representing the ascent and descent processes, respectively. Lidar observations (Fig. 6(d)) reveal that on 28 June, aerosols exhibited a distinctly stratified vertical structure,

Optics EXPRESS

particularly during the balloon ascent. As shown in Fig. 8, the spatial and temporal distribution of aerosols varied considerably during the 40-minute ascent of the tethered balloon, resulting in large variability in the inversion results at specific heights (e.g., 280 m and 780 m). Tethered balloon measurements generally match the lidar-retrieved mean profiles, staying mostly within the standard deviation range. In particular, the lidar-retrieved AAC profiles during the ascent process are better fitted to the actual observations. It is also noted that the inversion results near the surface exhibit the highest consistency for both ascent and descent, which may be due to more stable meteorological conditions.

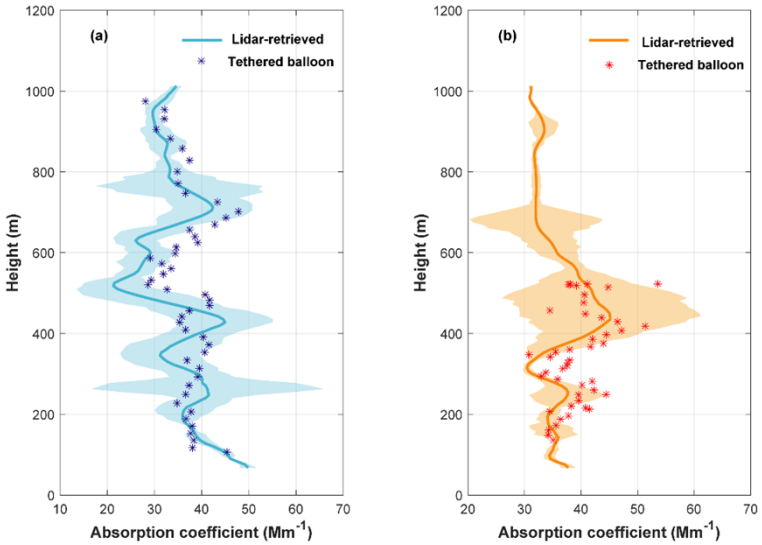

Fig. 8. Vertical structure of AAC on June 28, 2022. (Note: The solid lines represent the lidar-retrieved AAC profiles retrieved by PSO-GPR model during ascent (blue) and descent (orange) phases. Shaded regions represent the standard deviation of the inversion results.)

On 30 June (Fig. 9), during the ascent, the lidar-retrieved AACs exhibit strong agreement with tethered balloon observations below 300 m and above 700 m. Between 400 m and 600 m, most balloon observations fall within the shaded uncertainty range. Moreover, the mean lidar-retrieved AAC profile is lower than the observations, indicating an underestimation in the retrieval results. During the descent (Fig. 9(b)), the lidar-retrieved AACs show good agreement with the observations below 200 m near the surface. However, significant differences were observed within the 200–400 m layer, indicating notable changes in aerosol distribution during the descent. The third tethered balloon sounding experiment was conducted on the morning of July 2 and is shown in Fig. 10. Above 300 m, the lidar-retrieved AACs agree well with the sounding observations. Below 300 m, especially near the surface, there is a clear difference between the two. However, the overall vertical trend is still consistent.

To further evaluate the performance of the PSO-GPR model in retrieving AAC from lidar measurements, a validation dataset of 1,060 observation points was used, including 1,000 ground-based points (red dots) and 60 tethered balloon points (black triangles) in Fig. 11. The inversion performance on the validation dataset was slightly lower than that of the training dataset, yielding an overall R^2 of 0.86, indicating good agreement between observed and lidar-retrieved AACs. Some underestimation was observed, particularly in the range of 25-40 Mm^{-1}, where many points fell below the reference line (y = x). Tethered balloon observations mainly ranged from 15 to 35 Mm^{-1}, with $R^2 = 0.74$ and an RMSE of 4.25 Mm^{-1}, whereas ground-based observations were

Optics EXPRESS

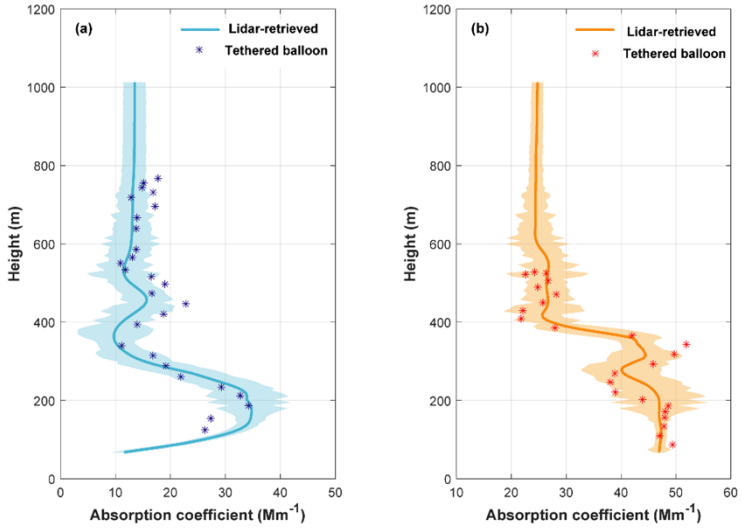

Fig. 9. Same as Fig. 8 but for June 30, 2022. (Note: The solid lines represent the lidar-retrieved AAC profiles retrieved by PSO-GPR model during ascent (blue) and descent (orange) phases. Shaded regions represent the standard deviation of the inversion results.)

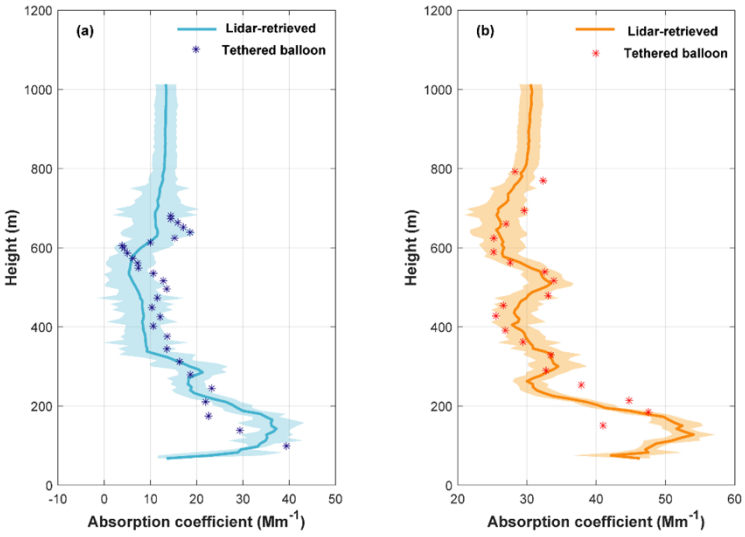

Fig. 10. Same as Fig. 8 but for July 2, 2022. (Note: The solid lines represent the lidar-retrieved AAC profiles retrieved by PSO-GPR model during ascent (blue) and descent (orange) phases. Shaded regions represent the standard deviation of the inversion results.)

Optics EXPRESS

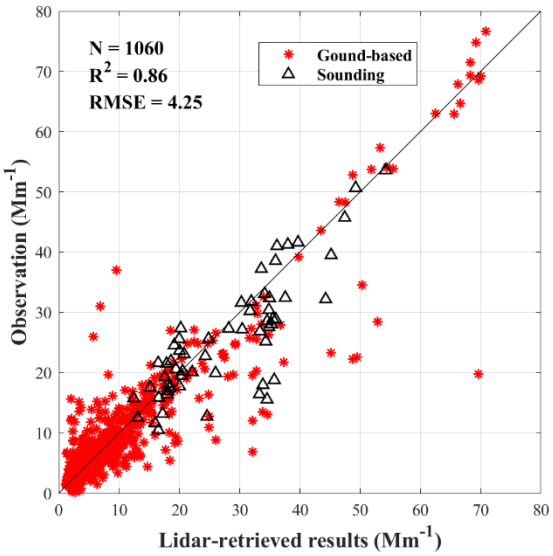

Fig. 11. Comparison of lidar-retrieved AAC with independent observational results from co-located ground-based Aethalometer and MA200 carried by tethered balloon.

mostly below 20 Mm^{-1}, with the lidar-retrieved results showing high consistency ($R^2 = 0.85$) and only a few significant deviations.

These results demonstrate that the PSO-GPR model is effective in retrieving AAC from dual-polarization lidar data. The model also fully exploits the vertical profiling capability of lidar to produce high-resolution AAC profiles with both fine spatial and temporal resolution.

4. Conclusions

In this study, we developed a new approach to retrieving vertical profiles of AAC from dual-polarization lidar measurements at 355 nm and 532 nm. The method integrates in-situ observations from ground-based AAC sensors and tethered balloon experiments with a hybrid machine learning framework combining particle swarm optimization and Gaussian process regression (PSO-GPR). This framework enables robust, high-resolution AAC retrievals across varying atmospheric conditions. The developed approach performs well, achieving R^2 values above 0.90 for both training and testing datasets, with near-surface AAC showing strong agreement with co-located Aethalometer measurements ($R^2 = 0.85$). Comparisons with tethered balloon profiles further validate the approach, with R^2 reaching 0.74.

This work provides a practical, scalable methodology for obtaining range-resolved AAC profiles with high spatial and temporal resolution. By accurately capturing the vertical structure of aerosol optical properties, the method enhances understanding of aerosol–radiation interactions and supports improved assessment of aerosol-induced climate effects. The combination of advanced machine learning and high-resolution lidar observations offers a powerful tool for atmospheric and climate research. The current model was trained using datasets from Northwest China, where dust and continental aerosols predominate. While the proposed PSO-GPR framework is methodologically universal, its direct application to regions with distinct aerosol compositions may require retraining or transfer learning strategies using local datasets to ensure optimal performance. Future work will focus on expanding the training dataset to cover broader temporal and spatial scales to improve global generalization.

Funding. National Natural Science Foundation of China (W2411029); Gansu Science and Technology Major Program

Optics EXPRESS

(24ZDWA006); Self-supporting Program of Guangzhou Laboratory (GZNL2024A01004); the '111 Center' (B25040); Fundamental Research Funds for the Central Universities (lzujbky-2025-jdzx04, lzujbky-2023-it09).

Acknowledgment. The authors greatly acknowledge the support of the Supercomputing Center of Lanzhou University, China.

Disclosures. The authors declare no conflicts of interest.

Data availability. Data underlying the results presented in this paper are not publicly available at this time but may be obtained from the authors upon reasonable request.

References

1. R. J. Charlson, S. E. Schwartz, J. M. Hales, *et al.*, "Climate Forcing by Anthropogenic Aerosols," Science **255**(5043), 423–430 (1992).
2. J. Haywood and O. Boucher, "Estimates of the direct and indirect radiative forcing due to tropospheric aerosols: A review," Rev. Geophys. **38**(4), 513–543 (2000).
3. S. Menon, J. Hansen, L. Nazarenko, *et al.*, "Climate Effects of Black Carbon Aerosols in China and India," Science **297**(5590), 2250–2253 (2002).
4. M. Z. Jacobson, "Control of fossil-fuel particulate black carbon and organic matter, possibly the most effective method of slowing global warming," J. Geophys. Res. **107**(D19), ACH 16-1 (2002).
5. E. M. Wilcox, R. M. Thomas, P. S. Praveen, *et al.*, "Black carbon solar absorption suppresses turbulence in the atmospheric boundary layer," Proc. Natl. Acad. Sci. U.S.A. **113**(42), 11794–11799 (2016).
6. L. Ran, Z. Z. Deng, P. C. Wang, *et al.*, "Black carbon and wavelength-dependent aerosol absorption in the North China Plain based on two-year aethalometer measurements," Atmos. Environ. **142**, 132–144 (2016).
7. K. A. Prather, "Our Current Understanding of the Impact of Aerosols on Climate Change," ChemSusChem **2**(5), 377–379 (2009).
8. R. N. C. Latimer and R. V. Martin, "Interpretation of measured aerosol mass scattering efficiency over North America using a chemical transport model," Atmos. Chem. Phys. **19**(4), 2635–2653 (2019).
9. R. Höller, "Wavelength-dependent aerosol single-scattering albedo: Measurements and model calculations for a coastal site near the Sea of Japan during ACE-Asia," J. Geophys. Res. **108**(D23), 2635 (2003).
10. Y. Gao, M. Zhang, Z. Liu, *et al.*, "Modeling the feedback between aerosol and meteorological variables in the atmospheric boundary layer during a severe fog–haze event over the North China Plain," Atmos. Chem. Phys. **15**(8), 4279–4295 (2015).
11. S. N. Tripathi, "Aerosol black carbon radiative forcing at an industrial city in northern India," Geophys. Res. Lett **32**(8), L08802 (2005).
12. J. Tao, L. Zhang, J. Cao, *et al.*, "A review of current knowledge concerning PM2. 5 chemical composition, aerosol optical properties and their relationships across China," Atmos. Chem. Phys. **17**(15), 9485–9518 (2017).
13. J. Xu, J. Tao, R. Zhang, *et al.*, "Measurements of surface aerosol optical properties in winter of Shanghai," Atmos. Res. **109-110**, 25–35 (2012).
14. T. C. Bond, G. Habib, and R. W. Bergstrom, "Limitations in the enhancement of visible light absorption due to mixing state," J. Geophys. Res **111**(D20), 20211 (2006).
15. R. Solanki and N. Singh, "LiDAR observations of the vertical distribution of aerosols in free troposphere: Comparison with CALIPSO level-2 data over the central Himalayas," Atmos. Environ. **99**, 227–238 (2014).
16. R. Solanki and N. Singh, "Climatology of aerosol radiative properties in the free troposphere," Atmos. Res. **102**(4), 365–393 (2011).
17. T. Mian Chin, O. Diehl, T. F. Dubovik, *et al.*, "Light absorption by pollution, dust, and biomass burning aerosols: a global model study and evaluation with AERONET measurements," Ann. Geophys. **27**(9), 3439–3464 (2009).
18. I. N. Sokolik and O. B. Toon, "Incorporation of mineralogical composition into models of the radiative properties of mineral aerosol from UV to IR wavelengths," J. Geophys. Res **104**(D8), 9423–9444 (1999).
19. A. Virkkula, N. C. Ahlquist, D. S. Covert, *et al.*, "A Three-Wavelength Optical Extinction Cell for Measuring Aerosol Light Extinction and Its Application to Determining Light Absorption Coefficient," Aerosol Sci. Technol. **39**(1), 52–67 (2005).
20. X. Guan, M. Wang, T. Du, *et al.*, "Wintertime aerosol optical properties in Lanzhou, Northwest China: Emphasis on the rapid increase of aerosol absorption under high particulate pollution," Atmos. Environ. **246**, 118081 (2021).
21. W. P. Arnott, K. Hamasha, H. Moosmüller, *et al.*, "Towards Aerosol Light-Absorption Measurements with a 7-Wavelength Aethalometer: Evaluation with a Photoacoustic Instrument and 3-Wavelength Nephelometer," Aerosol Sci. Technol. **39**(1), 17–29 (2005).
22. P. McMurry, "A review of atmospheric aerosol measurements," Atmos. Environ. **34**(12-14), 1959–1999 (2000).
23. B. H. Samset, G. Myhre, M. Schulz, *et al.*, "Black carbon vertical profiles strongly affect its radiative forcing uncertainty," Atmos. Chem. Phys. **13**(5), 2423–2434 (2013).
24. M. Kezoudi, C. Keleshis, P. Antoniou, *et al.*, "The Unmanned Systems Research Laboratory (USRL): A New Facility for UAV-Based Atmospheric Observations," Atmosphere **12**(8), 1042 (2021).
25. W. Zhu, Q. Liu, and Y. Wu, "Aerosol absorption measurement at SWIR with water vapor interference using a differential photoacoustic spectrometer," Opt. Express **23**(18), 23108 (2015).
26. Z. Huang, J. B. Nee, C. W. Chiang, *et al.*, "Real-time observations of dust-cloud interactions based on polarization and Raman lidar measurements," Remote Sens-Basel **10**(7), 1017 (2018).

Optics EXPRESS

27. Z. Huang, Q. Dong, B. Chen, *et al.*, "Method for retrieving range-resolved aerosol microphysical properties from polarization lidar measurements," Opt. Express **31**(5), 7599 (2023).
28. T. Wang, Y. Han, W. Hua, *et al.*, "Profiling dust mass concentration in northwest china using a joint lidar and sun-photometer setting," Remote Sens-Basel **13**(6), 1099 (2021).
29. Z. Huang, S. Qi, T. Zhou, *et al.*, "Investigation of aerosol absorption with dual-polarization lidar observations," Opt. Express **28**(5), 7028 (2020).
30. L. Abualigah, "Particle Swarm Optimization: Advances, Applications, and Experimental Insights," Comput., Mater. & Continua **82**(2), 1539–1592 (2025).
31. Y. Yoshikawa and T. Iwata, "Gaussian Process Regression With Interpretable Sample-Wise Feature Weights," IEEE Trans. Neural Netw. Learning Syst. **34**(9), 5789–5803 (2023).
32. H. Zhongwei, W. Yongkai, B. Jianrong, *et al.*, "An overview of aerosol lidar: Progress and prospect," National Remote Sensing Bulletin **26**(5), 834–851 (2022).
33. I. Mattis, A. Ansmann, D. Müller, *et al.*, "Dual-wavelength Raman lidar observations of the extinction-to-backscatter ratio of Saharan dust," Geophys. Res. Lett **29**(9), 20 (2002).
34. Z. Zhang, J. Huang, B. Chen, *et al.*, "Three-Year Continuous Observation of Pure and Polluted Dust Aerosols Over Northwest China Using the Ground-Based Lidar and Sun Photometer Data," J. Geophys. Res. Atmos **124**(2), 1118–1131 (2019).
35. G. S. W. Hagler, T. L. B. Yelverton, R. Vedantham, *et al.*, "Post-processing Method to Reduce Noise while Preserving High Time Resolution in Aethalometer Real-time Black Carbon Data," Aerosol Air Qual. Res. **11**(5), 539–546 (2011).
36. A. D. A. Hansen, H. Rosen, and T. Novakov, "The aethalometer — An instrument for the real-time measurement of optical absorption by aerosol particles," Sci. Total Environ. **36**, 191–196 (1984).
37. E. P. Blanco-Donado, I. L. Schneider, P. Artaxo, *et al.*, "Source identification and global implications of black carbon," Geosci. Front. **13**(1), 101149 (2022).
38. X. Liu, X. Zhang, J. Schnelle-Kreis, *et al.*, "Spatiotemporal Characteristics and Driving Factors of Black Carbon in Augsburg, Germany: Combination of Mobile Monitoring and Street View Images," Environ. Sci. Technol. **55**(1), 160–168 (2021).
39. P. B. Russell, R. W. Bergstrom, Y. Shinozuka, *et al.*, "Absorption Angstrom Exponent in AERONET and related data as an indicator of aerosol composition," Atmos. Chem. Phys. **10**(3), 1155–1169 (2010).
40. A.-P. Hyvärinen, V. Vakkari, L. Laakso, *et al.*, "Correction for a measurement artifact of the Multi-Angle Absorption Photometer (MAAP) at high black carbon mass concentration levels," Atmos. Meas. Tech. **6**(1), 81–90 (2013).
41. A. Petzold and M. Schönlinner, "Multi-angle absorption photometry—a new method for the measurement of aerosol light absorption and atmospheric black carbon," J. Aerosol Sci. **35**(4), 421–441 (2004).
42. L. Drinovec, G. Močnik, P. Zotter, *et al.*, "The "dual-spot" Aethalometer: an improved measurement of aerosol black carbon with real-time loading compensation," Atmos. Meas. Tech. **8**(5), 1965–1979 (2015).
43. L. Ferrero, V. Bernardoni, L. Santagostini, *et al.*, "Consistent determination of the heating rate of light-absorbing aerosol using wavelength- and time-dependent Aethalometer multiple-scattering correction," Sci. Total Environ. **791**, 148277 (2021).
44. A.-P. Hyvärinen, P. Kolmonen, V.-M. Kerminen, *et al.*, "Aerosol black carbon at five background measurement sites over Finland, a gateway to the Arctic," Atmos. Environ. **45**(24), 4042–4050 (2011).
45. R. Hitzenberger, A. Petzold, H. Bauer, *et al.*, "Intercomparison of Thermal and Optical Measurement Methods for Elemental Carbon and Black Carbon at an Urban Location," Environ. Sci. Technol. **40**(20), 6377–6383 (2006).
46. C. E. Rasmussen and C. K. I. Williams, *Gaussian Processes for Machine Learning* (The MIT Press, 2005).
47. F. Taher-Ghahramani, F. Zheng, and A. Eisfeld, "Gaussian process regression for absorption spectra analysis of molecular dimers," Spectrochim. Acta, Part A **275**, 121091 (2022).
48. J. Kennedy and R. Eberhart, "Particle swarm optimization," in *Proceedings of ICNN'95 - International Conference on Neural Networks* (1995), 4, pp. 1942–1948.
49. A. P. Piotrowski, J. J. Napiorkowski, and A. E. Piotrowska, "Particle Swarm Optimization or Differential Evolution—A comparison," Eng. Appl. Artif. Intell **121**, 106008 (2023).
50. S. Rana, S. Jasola, and R. Kumar, "A review on particle swarm optimization algorithms and their applications to data clustering," Artif. Intell. Rev **35**(3), 211–222 (2011).
51. H.-M. Lu, J.-S. Chen, and W.-C. Liao, "Nonparametric Regression via Variance-Adjusted Gradient Boosting Gaussian Process Regression," IEEE Trans. Knowl. Data Eng. **33**(6), 2669–2679 (2021).
52. H. Yan, K. Liu, C. Xu, *et al.*, "A novel method for identifying geomechanical parameters of rock masses based on a PSO and improved GPR hybrid algorithm," Sci. Rep. **12**(1), 5670 (2022).
53. J. Guo, F. Chen, and C. Xu, "Traffic Flow Forecasting for Road Tunnel Using PSO-GPR Algorithm with Combined Kernel Function," Math. Probl. Eng **2017**(1), 2090783 (2017).
54. J. Liu, "Enhanced prediction of bolt support drilling pressure using optimized Gaussian process regression," Sci. Rep. **14**(1), 2247 (2024).
55. D. Koch and A. D. Del Genio, "Black carbon semi-direct effects on cloud cover: review and synthesis," Atmos. Chem. Phys. **10**(16), 7685–7696 (2010).
56. D. V. Spracklen, K. S. Carslaw, U. Pöschl, *et al.*, "Global cloud condensation nuclei influenced by carbonaceous combustion aerosol," Atmos. Chem. Phys. **11**(17), 9067–9087 (2011).